# Supplemental Material: Measuring topological invariants in a polaritonic analog graphene

P. St-Jean,[1] A. Dauphin,[2] P. Massignan,[2,3] B. Real,[4] O. Jamadi,[4] M. Milićević,[1] A. Lemaître,[1] A. Harouri,[1] L. Le Gratiet,[1] I. Sagnes,[1] S. Ravets,[1] J. Bloch,[1] and A. Amo[4]

[1]*Centre de Nanosciences et de Nanotechnologies (C2N), CNRS - Universit Paris-Sud / Paris-Saclay, Palaiseau, France*

[2]*ICFO-Institut de Ciencies Fotoniques, The Barcelona Institute of Science and Technology, Barcelona, Spain*

[3]*Departament de Fsica, Universitat Politcnica de Catalunya, Barcelona, Spain*

[4]*Physique des Lasers, Atomes et Molcules (PhLAM), CNRS - Universit de Lille, Lille, France*

(Dated: February 19, 2021)

## I. SAMPLE AND EXPERIMENTAL DETAILS

### A. Sample description and experimental technique

The lattices are etched out of a planar semiconductor cavity with high quality factor ($Q \sim 70000$) consisting of a $Ga_{0.05}Al_{0.95}As$ $\lambda/2$ layer embedded between two $Ga_{0.05}Al_{0.95}As/Ga_{0.2}Al_{0.8}As$ Bragg mirrors formed from 28 (40) pairs in the top (bottom) mirror. Three sets of four GaAs quantum wells of 7 nm width are grown at the three central maxima of the electromagnetic field in the cavity, resulting in strong photon-exciton coupling exhibiting a 15 meV Rabi splitting. The exciton-photon energy detuning is of $\delta = -14.5$ meV at $k_x = k_y = 0$.

After the epitaxy, the cavity is processed by electron beam lithography and dry etching to form 2-dimensional lattices of overlapping cylindrical micropillars. For the regular honeycomb lattice, the diameter of the pillars is 2.7 $\mu$m and centre-to-centre distance is 2.4 $\mu$m, allowing for the hopping of polaritons. For the compressed honeycomb lattice, the normal ($a$) and compressed ($a'$) centre-to-centre distances are respectively 2.4 $\mu$m and 1.7 $\mu$m.

Non-resonant PL measurements are realized with a single-mode CW laser at 745 nm. The emission is collected through a microscope objective and imaged on the entrance slit of a spectrometer coupled to a CCD camera with a spectral resolution of $\sim 30$ $\mu$eV, using the experimental setup depicted in Fig. 2 (c) of the main text. The sample is cooled down at T = 4 K.

### B. Deviation from chiral symmetry

The band structures presented in this work always exhibit a small yet non-negligible deviation from chiral symmetry (i.e. the bands are not perfectly symmetric around a middle energy). This effect has already been observed in previous works involving lattices similar to those used in this work (e.g. Refs. [7] and [36]). It is explained by a slight deviation from the tight-binding approximation, as the $S-$ and $P-$ photonic orbitals of each pillar mix when they are put in contact. This mixing gives rise to an effective next-nearest-neighbour coupling whose amplitude has been estimated[1] to be around $0.07t$, where $t$ is the nearest-neighbour coupling energy.

However, it is important to point out that this effect does not play a significant role in our measurement of the winding number for two reasons: first, the next-nearest-neighbour coupling is relatively small; and second, as shown in Ref. [2], the necessary condition for the mean chiral displacement to converge toward $\mathcal{W}$ in a two-band model is the presence of inversion symmetry, a weaker condition than chiral symmetry, which is the case here (see discussion in Sec. VII of this Supplemental material). As a result, as shown in Sec. III of this Supplementals, the mean chiral displacement in lattices with long polariton lifetime indeed converges exactly (within the experimental error bars) to $\mathcal{W} = 0$ or 1, even if strict chiral symmetry is not fulfilled.

### C. Error analysis

Error bars shown in Figs. 3 and 4 of the main text are obtained by evaluating the standard deviation of the extracted mean chiral displacement over several repetitions of the same measurements. They are of the order of 0.08, and do not change significantly as a function of $k_x$.

On top of this statistical error, several points were subjected to a systematic error. This second type of error was associated to a slight vertical shift of the image on the CCD camera when laterally moving the cylindrical lens. This shift, typically on the order of few pixels (corresponding to $\sim 100$ nm), is most likely due to a slight misalignment in the imaging setup. In order to correct this effect when computing the mean chiral displacement, we have finely adjusted, for each $k_x$ point, the calibration relating the pixels of the camera to the imaged spatial position on the sample. This adjustment is necessary for properly defining the borders of each unit cell in Eq. 4 of the main text. Each calibration was done using spatially resolved photoluminescence (PL) spectra. Unadjusted data from Fig. 3 (c) of the main text, i.e. where the calibration is identical for each value of $k_x$, are presented in Fig. S1. We indeed see small systematic deviations of few clusters of points from the theoretical curve.

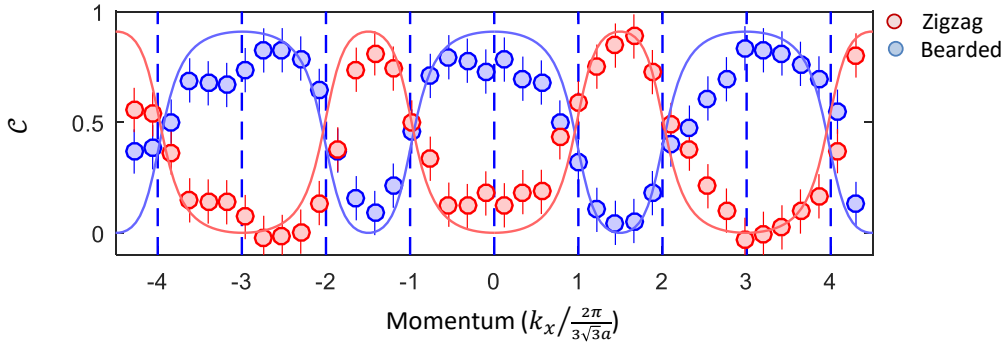


FIG. S1. Evolution of the mean chiral displacement as a function of $k_x$ for regular graphene. Identical to Fig. 3 (c) of the main text, but without using a correction on the definition of the unit cell for each value of $k_x$, i.e. the unit cell is identically defined for each point.

## II. TIME-INTEGRATED MEAN CHIRAL DISPLACEMENT

The definition of the mean chiral displacement used in Refs. 3 and 4 considers the *instantaneous* spatial profile of the Bloch modes in a 1D chiral lattice generated by a pulsed excitation:

$$\mathcal{C}(t) = \sum_i \langle \psi_i(t) | 2\hat{\Gamma}_i \hat{Y}_i | \psi_i(t) \rangle \tag{S.1}$$

where $|\psi_i(t)\rangle$ corresponds to the instantaneous amplitude of the wave-function at the position of the $i^{th}$ site, and $\hat{\Gamma}_i$ and $\hat{Y}_i$ refer to the sub-lattice and unit cell operators. These previous works showed that, in the long time limit (i.e. for $t \gg \hbar \langle j \rangle^{-1}$, where $\langle j \rangle$ is the average hopping amplitude of the SSH lattice), the instantaneous value of the mean chiral displacement converges toward the winding number. In this work, we consider time-integrated profiles of the Bloch modes under a CW excitation. We show hereafter that such steady-state values of $\bar{\mathcal{C}}$ as well lead to the winding number.

We consider the time-integrated mean chiral displacement :

$$\bar{\mathcal{C}} = \frac{1}{T} \int_0^T \mathcal{C}(t) dt = \int dy \; 2\Gamma(y) Y(y) I^{(\mathrm{int})}(y, k_x) \tag{S.2}$$

where $I^{(\mathrm{int})}(y, k_x)$ is the normalized time-integrated intensity for each point $y$ and $k_x$. $\Gamma(y)$ and $Y(y)$ are functions corresponding to the classical counterpart of $\Gamma_i$ and $Y_i$ operators.

For a 1D SSH lattice, this quantity can be readily computed using the following expression of the instantaneous mean chiral displacement derived in Ref. 3:

$$\mathcal{C}(t) = \mathcal{W} - \int_{-\pi}^{\pi} \frac{dk}{2\pi} \cos(2tE(k)) (\mathbf{n}(k) \times \partial_k \mathbf{n}(k))_z, \tag{S.3}$$

where $\mathcal{W}$ is the winding number, $E(k)$ is the energy dispersion, and $\mathbf{n}(k)$ is defined as:

$$H_{\mathrm{SSH}}(k) = E(k)\mathbf{n}(k)\cdot\boldsymbol{\sigma} \tag{S.4}$$

with $\boldsymbol{\sigma} = (\sigma_x, \sigma_y, \sigma_z)$ is the Pauli vector and $H_{\mathrm{SSH}}$ the 1D SSH Hamiltonian.

We find the following expression for $\bar{\mathcal{C}}$

$$\begin{aligned}\bar{\mathcal{C}} &= \mathcal{W} - \frac{1}{2\pi T}\int_{-\pi}^{\pi} dk\,(\mathbf{n}(k)\times\partial_k\mathbf{n}(k))_z \int_0^T dt\cos(2tE(k)) \\ &= \mathcal{W} - \frac{1}{2\pi T}\int_{-\pi}^{\pi} dk\,\frac{\sin(2TE(k))}{2E(k)}\,(\mathbf{n}(k)\times\partial_k\mathbf{n}(k))_z.\end{aligned} \tag{S.5}$$

In the limit of long integration times ($T\to\infty$), the second term in Eq. (S.5) rapidly vanishes and $\bar{\mathcal{C}}$ converges to the winding number $\mathcal{W}$. In the main text, $\bar{\mathcal{C}}$ is simply referred to as $\mathcal{C}$.

## III. TIME-INTEGRATED MEAN CHIRAL DISPLACEMENT IN A 1D SSH LATTICE

In order to experimentally benchmark this time-integrated version of the mean chiral displacement, we use a simple 1D lattice of coupled micropillars emulating the SSH Hamiltonian. This lattice is etched in a similar fashion to the honeycomb lattice in the main text. The pillars have a diameter of 3 $\mu$m and are separated by a distance alternating between 2.2 $\mu$m and 2.8 $\mu$m, in order to emulate the staggered hopping energies of the SSH Hamiltonian. A SEM image of this lattice is provided in Fig. S2 (a), and Fig. S2 (b) shows momentum-resolved emission spectra that clearly exhibit the two bands of the SSH model.

To extract the integrated mean chiral displacement in this lattice, we use a non-resonant CW excitation localized on a single pillar, similarly as described in the main text. Fig. S2 (c) shows an image of time-integrated emission spectra as a function of spatial position, which corresponds to the steady-state emission profile of the system. Above the panel, a schematic representation of the position of the different pillars is added with the pumped pillar in red. Fig. S2 (d) shows the emission integrated in energy over the two bands, and Fig. S2 (e) the spatial evolution of the function $\Gamma(y)Y(y)$ for both definitions of the unit cell: red corresponds to the topological phase (weak intra-cell coupling) and blue corresponds to the trivial phase (strong intra-cell coupling). This emission profile yields mean chiral displacement values of 0.98(8) and 0.05(8), thus demonstrating a rapid convergence toward the winding number values of 1 and 0.

This experimentally demonstrates the soundness of using the integrated mean chiral displacement for extracting the winding number of a chiral lattice.

## IV. TIME-INTEGRATED MEAN CHIRAL DISPLACEMENT WITH LOSSES

As pointed out in the manuscript, one critical aspect of 2D polaritonic lattices, with respect to 1D lattices such as the one considered above, is that the lifetime of polaritons becomes non-negligible compared to the hopping characteristic time. The difference in lifetimes comes from the etching technique of 2D lattices that is more aggressive than for 1D lattices, thus generating a higher density of non-radiative recombination centres at the surface of pillars.

This decreased lifetime leads to the fact that the mean chiral displacement does not converge to the exact values of the winding number, because polaritons do not have time to reach a perfectly balanced population over the two sub-lattices. Therefore, the emission profile does not reflect perfectly the chiral symmetry of the underlying array. Hereafter, we provide a numerical analysis showing how the extracted value of the mean chiral displacement depends on losses.

We simulate the decay of polaritons out of the cavity in the form of photons by considering a wave-function whose amplitude decays exponentially, following $e^{-\gamma t/2}$ where $\gamma$ is the polariton lifetime In this case, the integrated mean chiral displacement is:

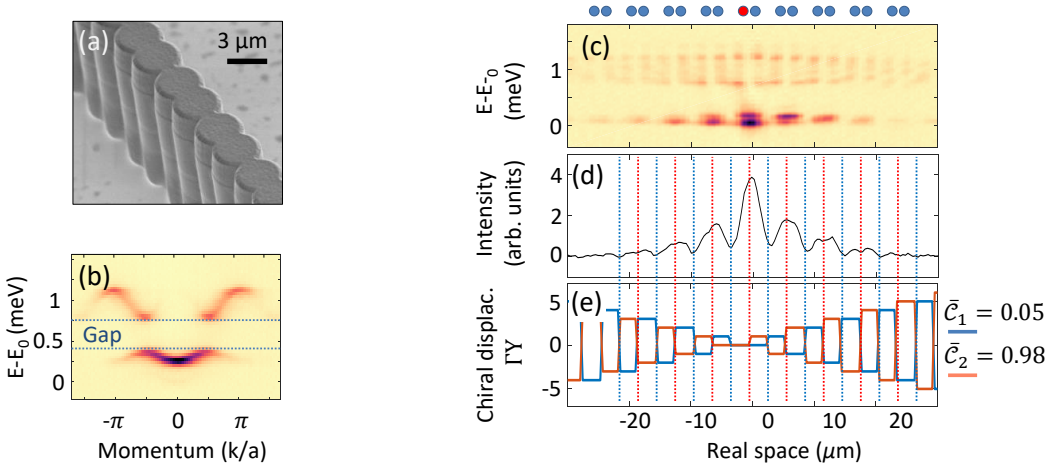


FIG. S2. (a) SEM image of a 1D lattice of coupled micropillars emulating the SSH Hamiltonian. (b) Momentum-resolved PL spectra. (c) Spatially resolved emission spectra under a non-resonant CW excitation localized on a single pillar. The position of the pump is indicated in red above the panel. (d) Energy-integrated emission profile. (e) Spatial evolution of the chiral displacement $\Gamma Y$. Blue and red curves are defined for a unit cell presenting a strong and weak intra-cell coupling, respectively.

$$\begin{aligned}
\bar{\mathcal{C}} &= \frac{1}{\int_0^T dt\langle\psi|\psi\rangle}\int_0^T dt\langle\psi|2\Gamma Y|\psi\rangle \\
&= \frac{1}{\int_0^T dt e^{-\gamma t}}\int_0^T dt\int_{-\pi}^{\pi}\frac{dk}{2\pi}e^{-\gamma t}(1-\cos(2tE(k)))(\mathbf{n}(k)\times\partial_k\mathbf{n}(k))_z \\
&= \mathcal{W} - \frac{1}{\int_0^T dt e^{-\gamma t}}\int_{-\pi}^{\pi}\frac{dk}{2\pi}(\mathbf{n}(k)\times\partial_k\mathbf{n}(k))_z\int_0^T e^{-\gamma t}\cos(2tE(k)) \\
&= \mathcal{W} - \frac{\gamma}{1-e^{-\gamma T}}\int_{-\pi}^{\pi}\frac{dk}{2\pi}e^{-\gamma T}\,\frac{\gamma e^{\gamma T}-\gamma\cos(2E(k)T)+2E(k)\sin(2E(k)T)}{\gamma^2+4E(k)^2}(\mathbf{n}(k)\times\partial_k\mathbf{n}(k))_z.
\end{aligned} \tag{S.6}$$

This formula has an asymptotic limit for $T\to\infty$:

$$\lim_{T\to\infty}\bar{\mathcal{C}} = \mathcal{W} - \frac{1}{2\pi}\int_{-\pi}^{\pi}dk\frac{\gamma^2}{\gamma^2+4E(k)^2}(\mathbf{n}(k)\times\partial_k\mathbf{n}(k))_z. \tag{S.7}$$

Figure S3 shows the computation of Eq. (S.7) as a function of losses ($\gamma/j$) for a SSH Hamiltonian with a coupling ratio of $j/j'=0.5$, where $j$ and $j'$ respectively correspond to intra- and inter-cell coupling energies. This case also corresponds to $k_x=0$ in graphene. It clearly shows a monotonous decay from $\mathcal{C}=1$ for a conservative system (i.e. $\gamma\to 0$), reaching a value of $\mathcal{C}=0.91$ for typical dissipation rates of 2D polaritonic lattices, i.e. $\gamma/j\sim 0.85$. This theoretical value agrees with the experimental one reported in the main text: $\mathcal{C}_{\rm exp}=0.84(8)$.

For comparison purposes, we also indicate the mean chiral displacement value expected for typical 1D lattices. In these lattices, the less aggressive etching techniques required in the fabrication process allows reaching longer polariton lifetimes ($\gamma/j\sim 0.1$). For such losses, the theoretical mean chiral displacement is very close to 1, which is in good agreement with the experimental values extracted in Fig. S2.

## V. EFFECT OF LOSSES IN POLARITONIC HONEYCOMB LATTICES

It is then possible to calculate the mean chiral displacement in a polariton honeycomb lattice (including losses) over the entire $k_x$ space by adapting Eq. (S.7) to:

$$\lim_{T\to\infty}\bar{\mathcal{C}}(k_x) = \mathcal{W}_{\rm HC}(k_x) - \frac{1}{2\pi}\int_{-\pi}^{\pi}dk_y\frac{\gamma^2}{\gamma^2+4E(\vec{k})^2}(\mathbf{n}(\vec{k})\times\partial_{k_y}\mathbf{n}(\vec{k}))_z, \tag{S.8}$$

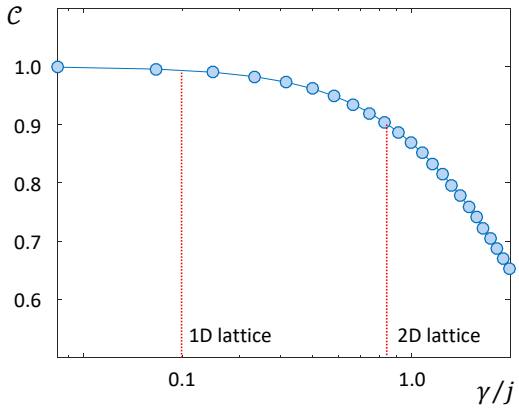


FIG. S3. Calculated mean chiral displacement as a function of losses ($\gamma/j$) for a bearded edge in graphene, at $k_x = 0$. The two red dashed lines indicated the typical values of losses for 1D and 2D polaritonic lattices.

with $E = E(\vec{k})$, the energy dispersion of graphene. Figures S4 (a) and (b) show the result of this equation for a ratio $\gamma/j \ll 1$ (i.e. negligible losses) and $\gamma/j = 0.85$ which is compatible with experimentally extracted values for the specific polaritonic honeycomb lattice used in this work, i.e. $\gamma = 150\ \mu eV$ and $j = 180\ \mu eV$.

The consequences of losses are twofold. First, the mean chiral displacements never reaches unity, but a maximum value of $\bar{\mathcal{C}} = 0.91$. Second, the evolution of the mean chiral displacement is less abrupt when crossing the Dirac cones (indicated by dashed lines). Both these effects are visible in measured values presented in the main text: the curve in Fig. S4 (b) corresponds to the theoretical one provided in Fig. 4 (c) of the main text.

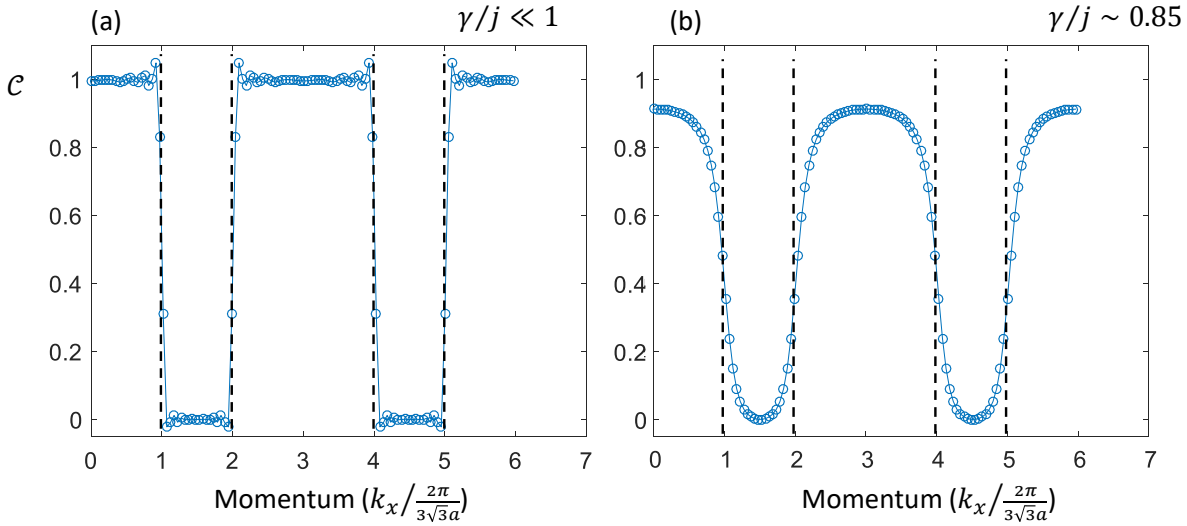


FIG. S4. (a) Integrated mean chiral displacement (over a time $T = 6\hbar/j$) in a honeycomb lattice as a function of momentum component $k_x$ for (a) negligible losses, and (b) losses compatible with a polaritonic honeycomb lattice ($t$ is the nearest neighbour coupling amplitude of the lattice).

## VI. EDGE STATES IN A REGULAR HONEYCOMB LATTICE

As mentioned in the main text, regular honeycomb lattices exhibit edge states for bearded and zigzag terminations at complementary positions in the BZ. The existence or absence of these edge states can be inferred through the measurement of the winding number in the bulk as is reported in this work. Confirmation of this existence of edge states can be obtained by measuring directly the emission spectrum along these edges. Such a measurement has already been reported in various platforms (see e.g. Refs. [6] and [7] of the main text). Hereafter, we provide such

complementary measurements for the specific lattices used in this work.

Figure S5 (a) and (b) present momentum-resolved PL spectra measured along a bearded and a zigzag termination. For this experiment, the excitation spot was centred on the edge row of the micropillar lattice, to excite the edge modes. Edge states (indicated by white curves/circles) are indeed observed in each case. Their position in the BZ is consistent with that expected from theory (see blue area in the sketches above each figure and in Fig. 1 (c) of the main text). Bulk modes are also excited and visible in the spectra (the blue lines are a guide for the eye associated to these modes).

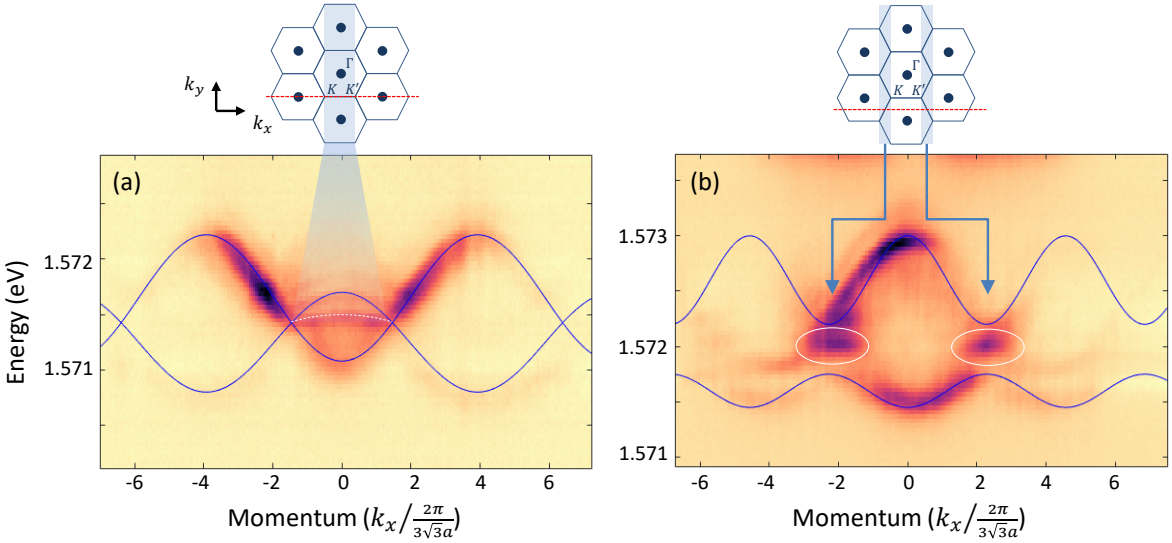


FIG. S5. PL emission spectra measured along a bearded (a) and zigzag (b) termination. For each case, the cut in the BZ along which the measurement is realized is schematically depicted above by a dashed red line. The theoretical positions at which the edge states are expected are indicated by blue areas (above Panel (a)) and blue arrows (above Panel (b)), and their corresponding positions experimentally measured are indicated in white on the figures, either with a white dashed line (Panel (a)) or white circles (Panel(b)).

## VII. MEAN CHIRAL DISPLACEMENT WITH INVERSION SYMMETRY

In the presence of a next-nearest neighbour hopping, graphene loses its chiral symmetry. In this way, the effective model we consider in this work changes topological class, going from a chiral symmetric topological phase characterized by a $\mathbb{Z}$ invariant, to an inversion symmetric phase characterized by a $\mathbb{Z}_2$ invariant. Nevertheless, it was shown in Ref. [2] that the topological invariant for a two-band system can still be computed through the *mean displacement* $\langle Y \rangle$ for a specific initial condition (completely localized on a single sublattice of a single unit cell). We show here that, more generally, the *mean chiral displacement* $\langle \Gamma Y \rangle$ measures the winding number of two-band inversion-symmetric systems for a generic initial condition localized within one unit cell.

The Hamiltonian of a two band system with inversion symmetry can be written as

$$H = \alpha(k)\,\mathbb{I} + \vec{n}\cdot\vec{\sigma} = \alpha(k)\,\mathbb{I} + H_\Gamma, \tag{S.9}$$

where the second term $H_\Gamma$ is a chiral Hamiltonian, meaning that $\{\Gamma, H_\Gamma\} = 0$ and therefore $\Gamma e^{-iH_\Gamma t}\Gamma = e^{iH_\Gamma t}$; the definition of $\Gamma$ is identical as in the main text. The chiral symmetry breaking term $\alpha(k)\,\mathbb{I}$ obviously commutes with $H_\Gamma$. As a consequence, $H$ and $H_\Gamma$ have the same eigenvectors and therefore the same Zak phase. This commutation relation also allows one to compute easily the mean chiral displacement $\mathcal{C}(t)$, which is the mean value of the operator $\Gamma Y$ given by the time evolution of an initial state localized on a single unit cell. In the presence of inversion symmetry,

one obtains

$$\begin{aligned}\mathcal{C}(t) &= \int_{-\pi}^{\pi} \frac{dk}{2\pi} \langle e^{iHt} \Gamma i\partial_k e^{-iHt} \rangle \\ &= \int_{-\pi}^{\pi} \frac{dk}{2\pi} \left[ \langle e^{iH_\Gamma t} \Gamma i\partial_k e^{-iH_\Gamma t} \rangle - \langle e^{iH_\Gamma t} \Gamma e^{-iH_\Gamma t} \rangle \partial_k \alpha \right] \\ &= \mathcal{C}_\Gamma(t) - \int_{-\pi}^{\pi} \frac{dk}{2\pi} \langle \Gamma e^{-2iH_\Gamma t} \rangle \partial_k \alpha.\end{aligned} \tag{S.10}$$

In the latter expression, the first term is the mean chiral displacement of the chiral part of the Hamiltonian $H_\Gamma$, which is known from previous works to converge to the desired invariant[3,4]. The second term is an extra contribution, which however is rapidly oscillating and vanishes in the long time limit[5]. Moreover, one can show that this extra term completely disappears when considering an initial condition being an eigenstate of the chiral operator or when tracing over a complete basis of initial conditions within the unit cell.

[1] F. Mangussi, M. Milićević, I. Sagnes, L. L. Gratiet, A. Harouri, A. Lema tre, J. Bloch, A. Amo, and G. Usaj, Journal of Physics Condensed Matter **32**, 315402 (2020).
[2] S. Longhi, Optics Letters **43**, 4639 (2018).
[3] F. Cardano, A. D'Errico, A. Dauphin, M. Maffei, B. Piccirillo, C. De Lisio, G. De Filippis, V. Cataudella, E. Santamato, L. Marrucci, M. Lewenstein, and P. Massignan, Nature Communications **8** (2017).
[4] M. Maffei, A. Dauphin, F. Cardano, M. Lewenstein, and P. Massignan, New Journal of Physics **20**, 013023 (2018).
[5] A. D'Errico, F. D. Colandrea, R. Barboza, A. Dauphin, M. Lewenstein, P. Massignan, L. Marrucci, and F. Cardano, Physical Review Research **2**, 023119 (2020).